Topological order and thermal equilibrium in polariton condensates
Supplementary Information

Davide Caputo,[1,2] Dario Ballarini,[1] Galbadrakh Dagvadorj,[3,4] Carlos Sánchez Muñoz,[5]
Milena De Giorgi,[1] Lorenzo Dominici,[1] Kenneth West,[6] Loren N. Pfeiffer,[6]
Giuseppe Gigli,[1,2] Fabrice P. Laussy,[7,8] Marzena H. Szymańska,[3] and Daniele Sanvitto[1,9]

[1] *CNR NANOTEC—Institute of Nanotechnology, Via Monteroni, 73100 Lecce, Italy*
[2] *University of Salento, Via Arnesano, 73100 Lecce, Italy*
[3] *Department of Physics and Astronomy, University College London,*
Gower Street, London WC1E 6BT, United Kingdom
[4] *Department of Physics, University of Warwick, Coventry CV4 7AL, United Kingdom*
[5] *CEMS, RIKEN, Saitama, 351-0198, Japan*
[6] *PRISM, Princeton Institute for the Science and Technology of Materials, Princeton Unviversity, Princeton, NJ 08540*
[7] *Faculty of Science and Engineering, University of Wolverhampton, Wulfruna St, WV1 1LY, United Kingdom*
[8] *Russian Quantum Center, Novaya 100, 143025 Skolkovo, Moscow Region, Russia*
[9] *INFN, Sez. Lecce, 73100 Lecce, Italy*

Sample and experimental setup

The sample used in this work is a high quality factor (Q>100000) GaAs/AlGaAs planar microcavity containing 12 GaAs quantum wells of 7 nm width, grouped in 3 blocks placed at the antinode positions of the electric field inside the cavity, with a collective Rabi splitting of $\hbar\Omega = 16$ meV. The front (back) mirror consists of 34 (40) pairs of AlAs/Al$_{0.2}$Ga$_{0.8}$As layers, with a polariton lifetime of about 100 ps [1]. The cavity detuning $\delta = \hbar(\omega_c - \omega_x)$ is slightly negative ($\delta = -1$ meV), with the exciton energy $\hbar\omega_x$=1611 meV. Photoluminescence measurements are performed in reflection configuration with the sample placed in the vacuum-chamber of a cryostat and kept at a temperature of about 10 K. Polaritons are non-resonantly excited by a single-mode Ti:sapphire laser in continuous wave (CW) operation with stabilized output wavelength and power (M2Squared SolsTis). To efficiently injects carriers in the structure, the energy of the pump is chosen to coincide with the first minimum of the reflection stop band (1686.80 meV). To avoid a possible thermal heating of the sample, the pump laser is chopped at a frequency of 4 kHz with a duty cycle of 8%. To obtain energy- and spatially-resolved information, an imaging spectrometer is coupled to the CCD detector as shown in Fig. S1.
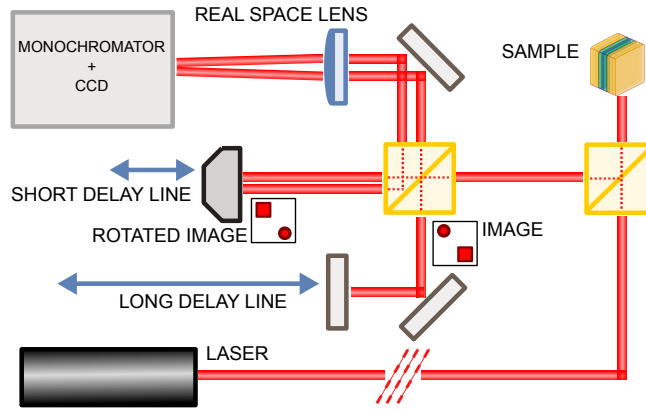

Figure S1: Scheme of the experimental setup with the Michelson interferometer in the detection line.

Interferometric measurements of first-order coherence

Moving a mirror in one arm of the interferometer by an automatised piezoelectric stage with a step size that is small compared to the wavelength, the sinusoidal envelope of the intensity versus the delay can be measured with high precision at each point of the interferogram as shown in Fig. S2. The first order correlation function is obtained as:

$$|g^{(1)}(\mathbf{r}, -\mathbf{r})| = V I_{\text{ideal}}, \tag{S1}$$

where $I_{\text{ideal}} = (I_1 + I_2)(2\sqrt{I_1 I_2})^{-1}$ takes into account small asymmetries between the two interferometer arms, with I_1 and I_2 the intensities in the two interferometer arms, while V is the visibility of the interference fringes. The
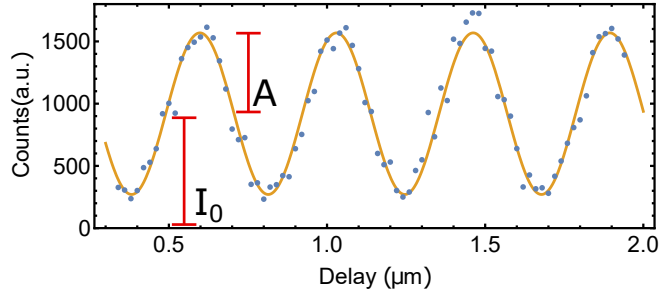
Figure S2: Sinusoidal envelope of the intensity on a single CCD pixel as a function of the piezo-controlled delay between the two arms of the interferometer.

visibility V is obtained by fitting the data, as shown in Fig. S2, with:

$$I(x) = I_0 + A\sin(\omega x + \phi_0) \tag{S2}$$

where $V = \frac{A}{I_0}$ and ϕ_0 is the initial phase. Alternatively, the 2D spatial coherence can be retrieved from the interferograms with standard Fast Fourier Transform algorithms, as in Fig. 2 of the main paper [2]. In the text the raw data are plotted without any normalization, and residual oscillations of the setup (cryostat, noise in the optical path, etc) can globally reduce the maximum coherence observed with time-averaged detection. This is taken into account by the space-independent amplitude parameter A in Eq. 1 and Eq. 2 of the main text. In Fig. 3 of the main text, integration times of 1100 ms, 1100 ms and 476 ms are used in the measurements of space correlations in panel a), b) and c), respectively. Temporal correlations of panels d), e) and f) have been recorded by averaging over 10 acquisitions of 300 ms, 300 ms and 100 ms, respectively.

Density of the polariton condensate

The contribution to the total density coming from different polariton states is energy-resolved by coupling the CCD detector to a spectrometer with a minimum step size of 10 μeV. This allows to measure the fraction of condensed polaritons with respect to the whole polariton population, as shown in Fig. S3a. The threshold density d_{th}, experimentally determined from the substantial increase in the lowest-energy population and the wider spatial coherence, corresponds to $\approx 20\%$ of polaritons in the lowest-energy state. In Fig. S3b, the population in the lowest energy state is calculated from numerical simulations as the ratio of polaritons with wave-vector $|k| < 0.1$ μm^{-1} with respect to the whole polariton population, in analogy to Fig. S3a. Remarkably, the fraction on polaritons in the ground state at d_{th} is almost identical for experiments and simulations. Moreover, $d_{th} \approx 1/3$ d_{BKT} and $\Delta E = g d_{BKT} = 50$ μeV, with g the interaction constant, for both numerical simulations and experiments.
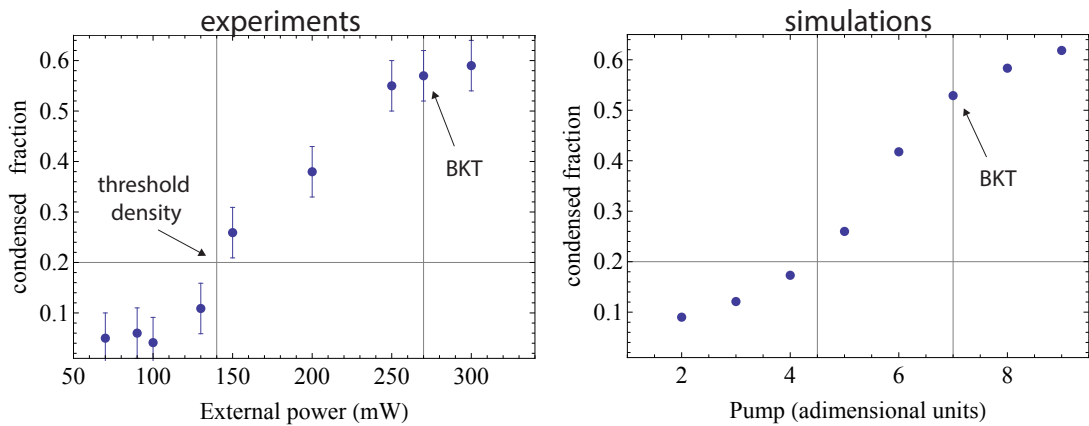

Figure S3: a, Ratio between the number of polaritons in the ground state and the whole polariton population as extracted from energy-resolved measurements. **b,** Fraction of polaritons at the bottom of the dispersion ($|k| < 0.1$ μm^{-1}) as obtained from numerical simulations.

The absolute polariton density d can be estimated using:

$$d = \frac{I\tau}{ES} \tag{S3}$$

where I is the intensity of the light emitted by the sample, τ the polariton lifetime, E the polariton energy and S the normalisation area. From Eq. S3 and Fig. S3a, the density at the BKT threshold can be estimated as $d_{BKT} \approx 0.8\ pol/\mu m^2$. However, the physics is actually described by the coupled energy terms $\Delta E = gd$, where d is the polariton density in the lowest-energy state and g is the interaction strength. While the absolute density value can be altered by additional losses in the mirrors or the substrate, the energy blueshift ΔE can be directly measured in a region far enough from the excitation spot to avoid the presence of uncoupled excitons. Comparing the blueshift with the density d_{BKT} calculated from Eq. S3, $g = 50\ \mu eV/\mu m^2$ is obtained, which is larger than expected. However, to avoid calibration issues and for sake of generality, only relative density values and the coupled product gd are used in the present discussion. Finally, the external power is used in Fig. S3 to graphically represent the increase of the condensed fraction, but polaritons are effectively pumped into the condensate through an expansion and relaxation process, retaining only an indirect relation with the external pumping power.

Velocity of the expanding polariton reservoir

The expansion of polaritons, accelerated outwards from the injection spot, acts as an effective polariton reservoir for the condensate at the bottom of the dispersion. The velocity of the expanding reservoir is almost constant in the range of powers considered and close to the maximum velocity achievable at this detuning. Indeed, the blueshift under the laser spot is above $3\,\mathrm{meV}$ for all the densities shown in Fig. 2 of the main text, corresponding to the blue points of Fig. S4a. The corresponding group velocity is actually slightly decreasing with power due to the nonparabolic curvature of the dispersion, as shown in Fig. S4b.
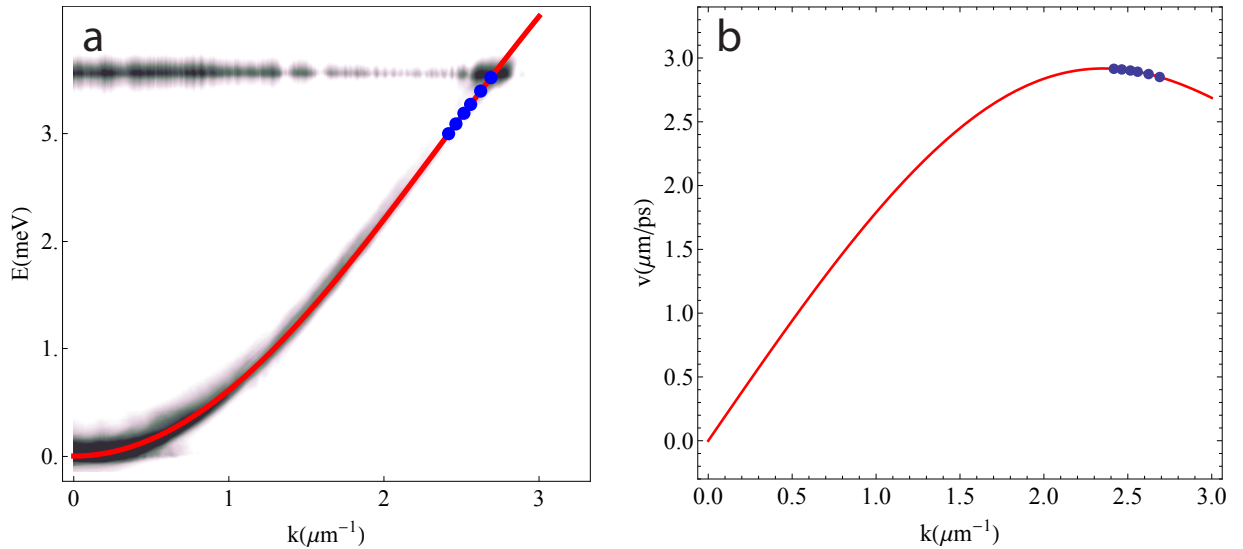

Figure S4: a, Polariton dispersion including the central spot, the expanding polariton reservoir and the bottom state. The blueshift corresponding to the excitation power used in Fig. 2(a-f) of the main text is indicated by blue dots. **b,** Group velocities corresponding to blue dots in **a** and to Fig. 2(a-f) of the main text.

Density profile versus spatial coherence

The polariton density is asymmetrically decaying in the region shown in Fig. 1(b-c) because it is radially expanding from the injection spot. In Fig. S5, the density profile, as obtained from photoluminescence measurements, is compared to the decay of spatial coherence with distance. Below threshold, the coherence shows a fast decay with distance (exponential or gaussian for blue and yellow curves, respectively), that becomes a stretched-exponential decay above threshold (green curve) and a power-law decay at higher densities (red curve). While the slope of the spatial density profile does not change significantly with power, giving the same exponential decay of $\sim$50 μm for all the curves shown in Fig. S5a, the difference in the coherence length is instead evident in Fig. S5b. Therefore, while the density is decreasing with distance, the spatial correlations follow the expected power law decay in the range of density where the BKT phase can be sustained. Even if the numerical model assumes a homogeneous system, the experimental

evidence is that non-local properties such as spatial correlations can be correctly reproduced within a homogeneous model with the same average healing length, even for sizable global density differences, at least for slow variations of the particle density in space.
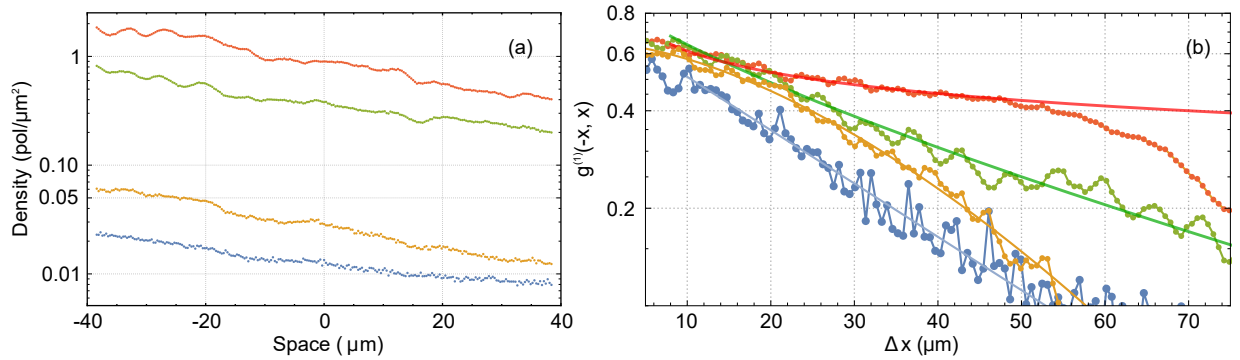

Figure S5: Spatial decay of intensity (**a**) and spatial decay of coherence (**b**) for different excitation powers corresponding to $d = (0.06, 0.15, 1.4, 2.75) \, d_{th}$.

Uniform phase

The phase of the polariton condensate can be extracted from the 2D interferogram obtained with a reference of constant phase. In this case, the retroreflector is not used and the reference is obtained by expanding a small region of the condensate itself. In Fig. S6a, the density of the polariton condensate in the region of interest is shown as a color map. The formation of a uniform phase, in the same spatial region shown Fig. S6a, is evident by comparing Fig. S6b (below threshold) with Fig. S6c (above threshold). The phase profile has a negligible gradient in the region of interest (Fig. S6e), corresponding to a mean global velocity $v < 0.1 \, \mu m/ps$ (Fig. S6f). This is compatible with $k < 0.1 \, \mu m^{-1}$, as also independently obtained from the measured polariton dispersion in the same spatial region (Fig. S6d).

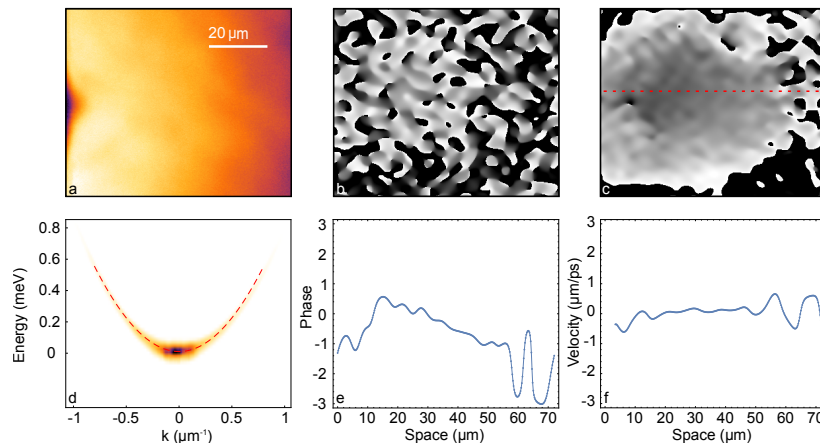**Figure S6: a,** Spatially resolved emission intensity of the polariton condensate (color scale). **b, c,** Phase in the same spatial region as in **a** for $d < d_{th}$ (**b**) and $d > d_{th}$ (**c**). Color scale goes from $-\pi$ (white) to $+\pi$ (black). Above threshold, a uniform phase is spontaneously formed within a wide spatial region. At larger distances, a rapidly varying phase is visible. A phase singularity, in this case pinned to a small defect, is also visible on the left of the figure. **d,** Polariton dispersion in the region of interest. The polariton emission is peaked around the $k = 0$ state at the bottom of the dispersion. **e,** Phase profile along the dashed-red line in **c**. **f,** Condensate velocity extracted from the gradient of the phase in **e**.

Healing length

The healing length, defined as:

$$\xi = \sqrt{\hbar^2/2mgd}, \qquad (S4)$$

with m the polariton mass, g the interaction constant and d the polariton density in the condensate, is shown in Fig. S7a as calculated from the experimental data. The polariton mass, obtained by fitting the polariton dispersion, is $m = 3.8 \times 10^{-5} m_e$, where m_e is the electron mass. The product gd is instead measured from the polariton blueshift. In Fig. S7b, the healing length obtained by numerical simulations is shown for comparison. The experimental and theoretical values are in good agreement, measuring an healing length ξ between $4 \; \mu m$ and $6 \; \mu m$ at the BKT point.
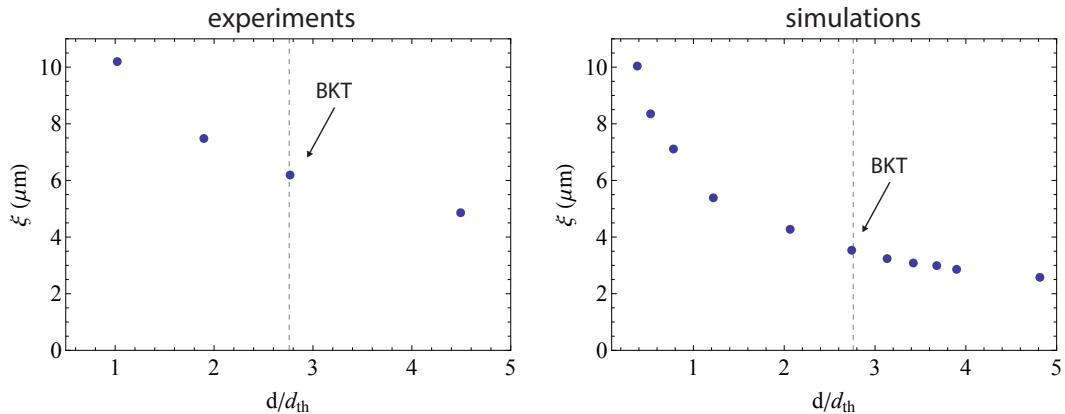

Figure S7: The healing length, as obtained from experiments (**a**) and simulations (**b**).

Coherence Length and Time

In order to evaluate the coherence length and time as a function of density in the whole range across the transition, both spatial $g^{(1)}(x, -x, t = 0)$ and temporal $g^{(1)}(t, t + \Delta t)$ are fitted with stretched-exponential functions as reported in Eq. 2 of the main text. It is therefore possible to define both in space and time the relaxation length (time) as:

$$\langle l \rangle = \int_0^\infty dx \, e^{-(x/l_e)^\beta} = \frac{l_e}{\beta} \Gamma \left(\frac{1}{\beta} \right) \tag{S5}$$

with l_e the renormalization factor scale of the x-axis and Γ the gamma function, with x-axis both the spatial and temporal one. The resulting coherence length and time are reported in Fig. S8.
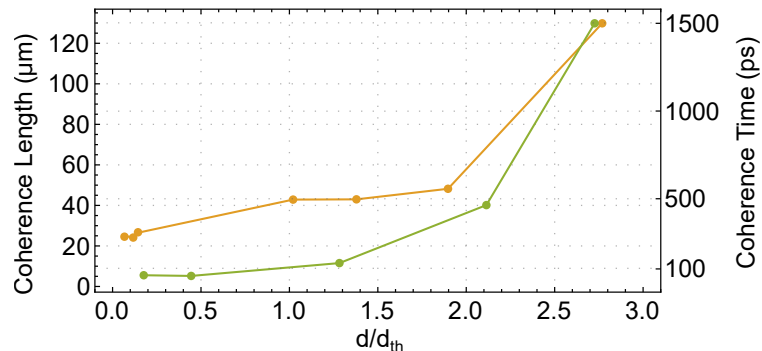

Figure S8: Coherence length (yellow) and time (green) for different densities extracted from the stretched exponential fitting.

Fitting Model and Residuals Analysis

The analysis of the fitting results allows to assess the applicability of the model used in the fitting procedure. In Fig. S9 we show the residuals of fitting the temporal first order correlation function $g^{(1)}(t, t + \Delta t)$ in the quasi-ordered regime (red square in Fig. 3h of the main paper). We report different attempts to fit the data using an exponential (blue, row (a)), a Gaussian (yellow, row (b)), a stretched exponential (green, row (c)) and a power law (red, row (d)). The P-P (Probability Probability) plot is a standard tool to investigate the deviance of a data set from the normal distribution.
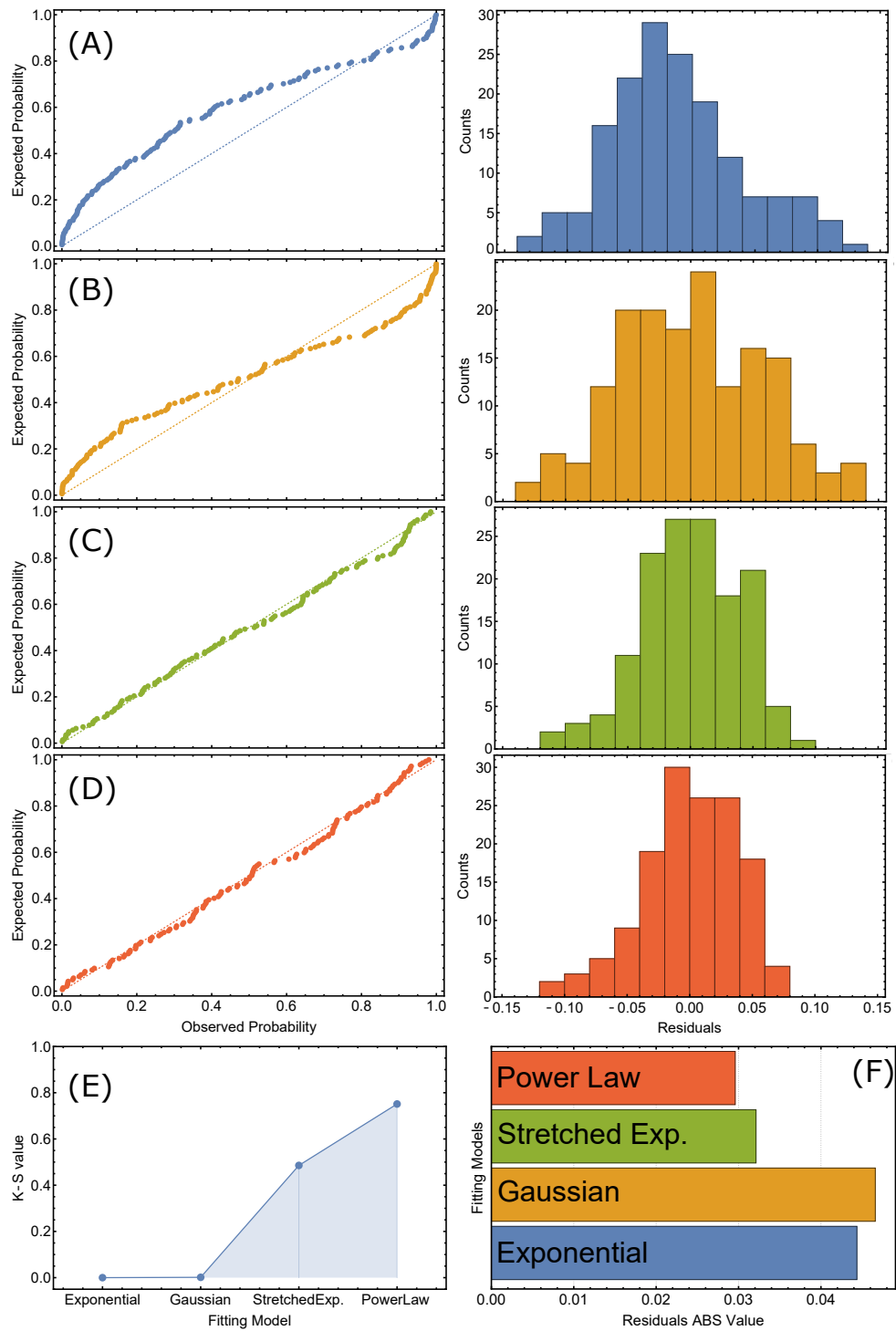
Figure S9: Fitting residuals analysis for the temporal algebraic regime (red square in Fig. 3h of the main text). Each color corresponds to a different model used to fit the temporal decay. Row **a**: P-P plot for the observed and expected Gaussian with minimum standard deviation of residuals distribution for the exponential model. Row b: Gaussian model. Row c: Stretched exponential model. Row d: Power law model. e: Kolmogorov-Smirnov value quantifying the normality of the residuals distribution for each model. f: Total Absolute Value of fitting residuals, normalised to the number of point used.

Figure S10: Fitting residuals analysis for the spatial algebraic regime (red square in Fig. 3g of the main text). Each color corresponds to a different model used to fit the spatial decay. Row a: P-P plot for the observed and expected Gaussian with minimum standard deviation of residuals distribution for the exponential model. Row b: Stretched exponential model. Row c: Ppower law model. d: Kolmogorov-Smirnov value quantifying the normality of the residuals distribution for each model. e: Total Absolute Value of fitting residuals, normalised to the number of point used.
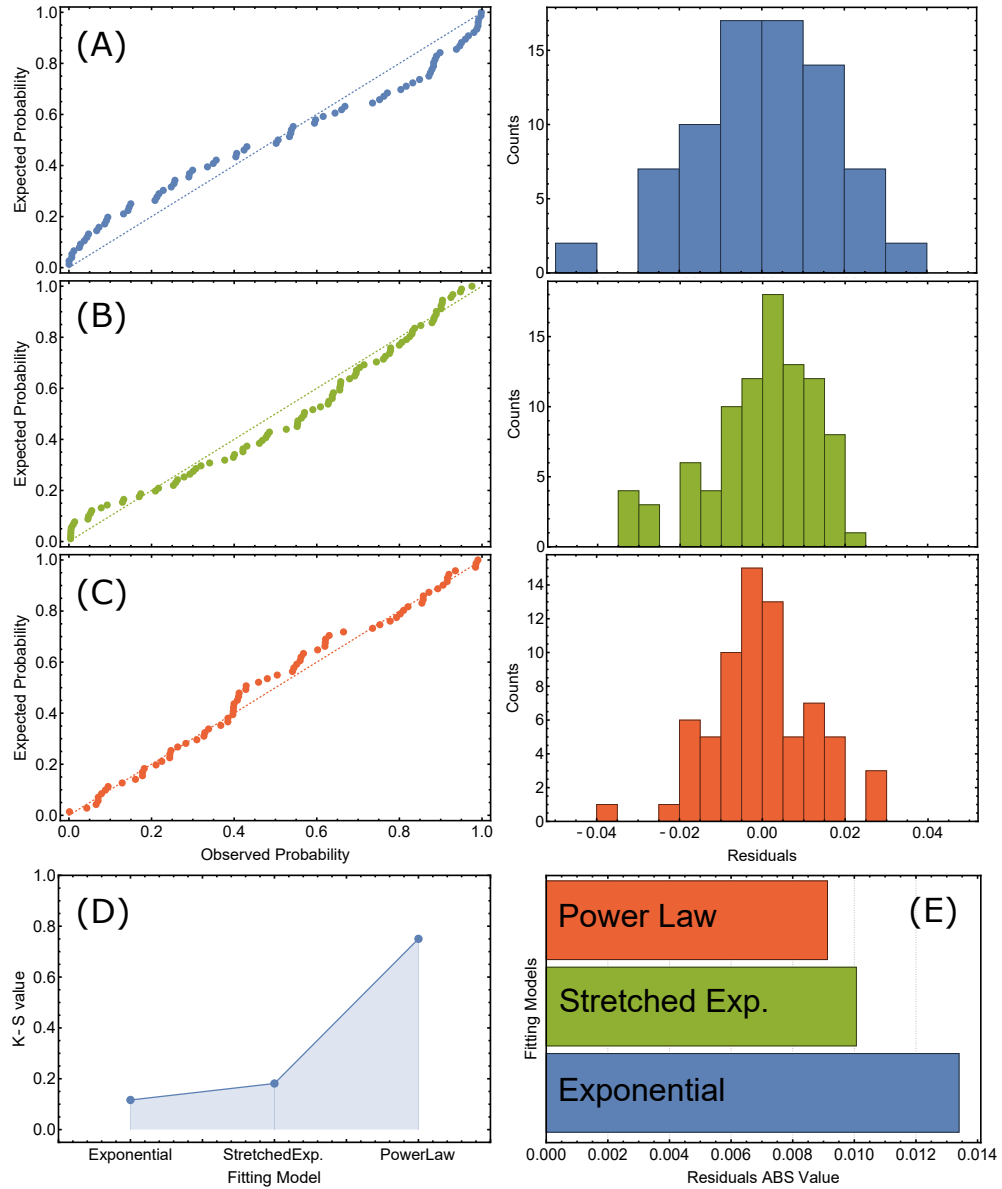
Indeed, fitting residuals with a normal distribution around the zero value represents a strong indication that the power-law model used to fit the data is the best one. The Kolmogorov-Smirnov test permits to quantitatively check the deviation from the normal distribution of a dataset. In order to assure that we have the minimum residual spreading, we used normalised Gaussian distributions with variance σ chosen for each model in order to best fit the data distribution. The value of this test, maximum for the power law model, combined with the fact (Fig. S9f) that the sum of the absolute values of the residuals is minimum for the power law model, confirms that the power law is the best fitting for the temporal decay of the correlation above BKT transition. In Fig. S10 we show the same analysis for the spatial decay of correlations (red square in Fig. 3g of the main paper). In this case the Gaussian fitting is not shown because the values of the residuals is too large.

Theoretical Description

In the classic equilibrium BKT scenario, for a system with linear dispersion in the ordered phase, we expect a slow algebraic decay (as Eq. 1 of the main text) of the first order coherence with exactly the same power-law exponents in *both* space (α_s) and time (α_t) [3, 4], given by $\alpha_{s,t} = k_B T / n_s$, where T indicates temperature and n_s the superfluid density. $\alpha_{s,t}$ have an upper bound of 1/4 [5] at which density/temperature vortices proliferate, causing an exponential decay of coherence, characteristic for the disordered phase. At the same time non-equilibrium dissipative driven systems, with diffusive spectrum in the ordered phase [3, 6], have been shown to still exhibit an algebraic decay of coherence *but* with temporal correlations decaying two times slower then the spatial ones $\alpha_t = 1/2 \, \alpha_s$ [3, 4]. Moreover, values of α_s as large as four times the equilibrium upper bound, when approaching the BKT transition, were reported both experimentally [7] and from theoretical analysis [8], using beyond-mean-field truncated Wigner methods able to account for vortices, suggesting an "over-shaken" superfluid state [8]. Finally, it has recently been suggested that the dissipation might in fact have an even more profound effect on the system with collective phase fluctuations destroying the algebraic order at long distances, leading to a stretched exponential decay of first order coherence characteristic of Kardar-Parisi-Zhang phase (KPZ)[9]. In that scenario the parameter β of the stretched exponential (see Eqn. (2) of the main paper) are also different for space ($\beta \approx 0.78$) and time ($\beta \approx 0.48$). Even if later estimates of the KPZ length-scales appeared to be unrealistic for incoherently driven microcavities with long lifetimes as in our case, and the presence of free topological defects strongly hampers the possibility of the KPZ phase [10], the true nature of the 2D exciton-polariton phase transition and the resulting order is still at the center of an intense debate. Additionally, the type of the Renormalisation-Group (RG) analysis, which led to those conclusions [9, 10], rely on the expansion in one over the mean-field density, and so are inadequate in describing the crossover region close to the phase transition. Thus, here, to specifically address the region close to the phase transition we restore to exact numerical solutions of the stochastic equations of motions, described in the next section.

Stochastic simulations

Our system consists of an ensemble of bosonic particles (the lower-polaritons) of mass m and lifetime 2κ, interacting via contact interactions g, and driven incoherently with pump of strength γ. The pumping saturation due to other processes is Γ. Note, that since our condensate forms in a reservoir-free region, we do not include any excitonic reservoir in the theoretical description. Also, in this work, our main focus is the formation of phase coherence in the lowest energy state at the bottom of the polariton dispersion, thus both in the experimental and in the theoretical investigations, our starting point is to examine polariton fluid after it has already expanded from the pumping spot, and the "condensate" has being fed from the incoherent polariton population after their expansion. We do not describe this expansion here neither theoretically nor experimentally. The details of relaxation via phonon-assisted scattering has been instead investigated in [1]. In our model the polariton decay rate is independent on their energy. However, the redistribution towards low energy modes is enabled by polariton-polariton interactions, which would lead to thermalisation in a closed system of bosons. Indeed, bosonic stimulation leads to an effective gain for k=0 and near-by modes. Combination of the facts that low energy modes get preferentially occupied while the decay is the same for all modes leads to a kind of effective cooling mechanism in this open system.

Using Keldysh field theory one can show that by including the classical fluctuations to all orders, but quantum fluctuations only to the second order (correct in the long-wavelength limit), and employing the Martin-Siggia-Rose formalism, one can arrive at the stochastic equation for the field $\psi(\mathbf{r}, t)$ (for a review see [11]). Alternative derivation, using the Fokker-Planck equation for the Wigner function, aimed at numerical implementation on a finite spatial grid dV, has been reviewed in [12]. The finite grid version reads

$$id\psi(\mathbf{r},t) = \left[-\frac{\nabla^2}{2m} + g|\psi(\mathbf{r},t)|_-^2 + i(\gamma - \kappa - \Gamma|\psi(\mathbf{r},t)|_-^2) \right] \psi(\mathbf{r},t)dt + dW \tag{S6}$$

where dW is the Wiener noise with correlations

$$\langle dW^*(\mathbf{r}',t)dW(\mathbf{r},t) \rangle = \frac{\gamma + \kappa + \Gamma|\psi(\mathbf{r},t)|^2}{dV} \delta_{\mathbf{r},\mathbf{r}'} dt,$$

where by $|\psi(\mathbf{r},t)|_-$ we abbreviated the following expression for the density $|\psi(\mathbf{r},t)|_- = |\psi(\mathbf{r},t)| - \frac{1}{dV}$, which comes from the Wigner function relating to the time symmetric and not time ordered operators. $\psi(\mathbf{r},t)$ contains both coherent (superfluid) and incoherent (normal) polaritons.

In Ref. [9], equations S6 are solved approximately analytically using RG analysis by eliminating the amplitude fluctuations, and focusing solely on the non-topological phase-fluctuations. The procedure, however, relies on an expansion in one over the mean-field density, which together with approximating the amplitude fluctuations and discarding vortices, cannot capture the region close to the phase transition. Instead, here, we solve this equation

exactly numerically on a finite grid. In addition, we have checked our results with a more general model of a saturable drive, applicable also to higher densities, in which $\gamma - \Gamma|\psi(\mathbf{r}, t)|^2_-$ in Eq. S6 is replaced by

$$\frac{\gamma}{1 + \frac{|\psi(\mathbf{r},t)|^2_-}{n_s}},$$ (S7)

with the noise strength proportional to

$$\frac{\gamma}{1 + \frac{|\psi(\mathbf{r},t)|^2_-}{n_s}} + \kappa.$$ (S8)

There is no appreciable difference between the results from the two models for our relatively low densities.

We evolve the dynamics of the stochastic equations (S6) with the XMDS2 software [13] using a fixed-step (to ensure stochastic noise consistency) 4th order Runge-Kutta (RK) algorithm, which we have tested against fixed-step 9th order RK, and a semi-implicit fixed-step algorithm with 3 and 5 iterations. We choose the system parameters to be the same as for experiments: the mass of the microcavity lower polaritons is taken to be $m = 3.8 \times 10^{-5} m_e$, where m_e is the electron mass, the polariton lifetime $2\kappa = 1/101.3 \ ps^{-1}$, and the polariton-polariton interaction strength $g = 0.004$ meVμm^2. The only parameter that is not possible to extract from the experiment is the saturation rate of the driving process (or in other words the three-body type losses in the system). We perform analysis for a range of Γ (or n_s) values, and since the other parameters are fixed, we choose the value of Γ (or n_s) that is able to reproduce the overall length scale of $g^{(1)}(x)$.

In our method, the stochastic averages over the configurations of different realisations of the fields provide the expectation value of the corresponding symmetrically ordered operators, and it is important to get the results to converge in the number of realisations. The first order spatial correlation function $g^{(1)}(x)$ is defined according to

$$g^{(1)}(r_1, t_1; r_2, t_2) = \frac{\langle \psi_1^* \psi_2 \rangle}{\sqrt{\langle \psi_1^* \psi_1 \rangle \langle \psi_2^* \psi_2 \rangle}}$$ (S9)

with ψ_i^* and ψ_i the creation and annihilation operators for the space-time point (r_i, t_i), with $i = 1, 2$, and it is evaluated by averaging over 100 independent stochastic paths, and additionally over auxiliary position in space r_0, since in simulations our system is uniform. The temporal correlation function is evaluated from a single spatial point (to avoid picking up any spatial correlations) after the steady-state is reached, and averaged over 10000 stochastic paths. Since the Wigner average provides the expectation value of the corresponding *symmetrically* (and not time)-ordered operators, we need to subtract the expectation value of the commutator. For single time correlation functions, such as $g^{(1)}(x)$, the commutator is simply $\frac{1}{2dV}$. For two-time correlation functions, such as $g^{(1)}(t)$, strictly speaking the expectation value of the commutator is unknown. It is, however, changing from $\frac{1}{2dV}$ at $t = 0$ to 0 at $t \to \infty$. Using the two limiting values allows us to estimate the error, which we expect to be small given the densities considered. Indeed, for the densities used here the difference is practically indistinguishable. In order to test the robustness of
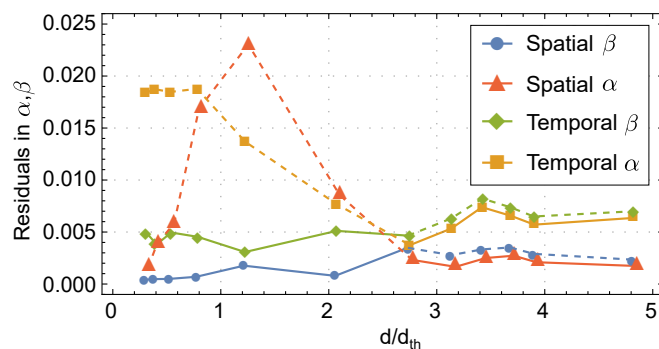

Figure S11: Residuals of the stretched exponential fit, β, for spatial (blue) and temporal (green) $g^{(1)}$, and the power-law fit, α, for spatial (red) and temporal (orange) $g^{(1)}$ as a function of the polariton density normalised to the BKT threshold.

our conclusions to the choice of the numerical parameters, we perform simulations on different spatial grids varying from 2 to 5 μm in the grid spacing, and different system sizes from 256 to 1024 μm. Note, that to satisfy the condition

necessary to derive the discrete version of equation (S6), $g/[(\kappa + \gamma)dV] \ll 1$, whilst maintaining a sufficient spatial resolution and, at the same time, a large enough momentum range, the window of available momentum grids is quite narrow. We find the main conclusions of our work (such as the crossover in $g^{(1)}(x)$ and $g^{(1)}(t)$ from exponential to power-law, spatial and temporal α being the same in the algebraic phase and smaller then $1/4$, as well as the behaviour of vortices) independent on the choice of those parameters. Here, we present a case with $2\,\mu m$ grid spacing, and system size of $256\,\mu m$, which is sufficiently larger from experimental to avoid any boundary effects influencing the relevant region. Finally, in order to assess which functional form fits the numerical data best we perform residuals analysis similar to those applied to experimental data. The residuals for the data and fittings presented in the main text is shown in Fig S11.

References

[1] D. Ballarini, D. Caputo, C. Muñoz, M. De Giorgi, L. Dominici, M. Szymańska, W. K., L. Pfeiffer, G. G., F. Laussy, et al. Phys. Rev. Lett. **118**, 215301 (2017).

[2] L. Dominici, M. Petrov, M. Matuszewski, D. Ballarini, M. De Giorgi,D. Colas, E. Cancellieri, B. Silva Fernandez, et al Nature Communications **6**, 8993 (2015).

[3] M. H. Szymanska, J. Keeling, and P. B. Littlewood, Phys. Rev. Lett. **96**, 230602 (2006).

[4] M. H. Szymańska, J. Keeling, and P. B. Littlewood, Phys. Rev. B **75**, 195331 (2007).

[5] D. R. Nelson and J. M. Kosterlitz, Phys. Rev. Lett. **39**, 1201 (1977).

[6] M. Wouters and I. Carusotto, Phys. Rev. A **76**, 043807 (2007).

[7] G. Roumpos, M. Lohse, W. H. Nitsche, J. Keeling, M. H. Szymanska, P. B. Littlewood, A. Löffler, S. Höfling, L. Worschech, A. Forchel, et al., Proceedings of the National Academy of Sciences **109**, 6467 (2012).

[8] G. Dagvadorj, J. M. Fellows, S. Matyjaskiewicz, F. M. Marchetti, I. Carusotto, and M. H. Szymanska, Phys. Rev. X **5**, 041028 (2015).

[9] E. Altman, L. M. Sieberer, L. Chen, S. Diehl, and J. Toner, Phys. Rev. X **5**, 011017 (2015).

[10] G. Wachtel, L. Sieberer, S. Diehl, and E. Altman, arXiv:1604.01042v2 (2016).

[11] L. M. Sieberer, M. Buchhold, S. Diehl, Rep. Prog. Phys. **79**, 096001 (2016).

[12] I. Carusotto and C. Ciuti, Rev. Mod. Phys. (2013), 1205.6500.

[13] G. R. Dennis, J. J. Hope, and M. T. Johnsson, Comput. Phys. Commun. **184**, 201 (2012), 1204.4255.